Automatic classification-based generation of thermal infrared land surface emissivity maps using AATSR data over Europe

Eduardo Caselles[1]

E-mail: eduardo.caselles@uv.es
Phone: +34 96 354 31 21
Fax: +34 96. 354 33 85
Permanent Address: Department of Earth Physics and Thermodynamics, Faculty of Physics, University of Valencia. C/ Dr. Moliner, 50. E - 46100 Burjassot, Spain.

Enric Valor[1], Francisco J. Abad[2], Vicente Caselles[1]

[1]*Department of Earth Physics and Thermodynamics, University of Valencia. C/ Dr. Moliner, 50. 46100 Burjassot, Spain.*

[2]*Department of Information Systems and Computation, Technical University of Valencia. Camino de Vera s/n. 46022 Valencia, Spain.*

ABSTRACT

The remote sensing measurement of land surface temperature from satellites provides a monitoring of this magnitude on a continuous and regular basis, which is a critical factor in many research fields such as weather forecasting, detection of forest fires or climate change studies, for instance. The main problem of measuring temperature from space is the need to correct for the effects of the atmosphere and the surface emissivity. In this work an automatic procedure based on the Vegetation Cover Method, combined with the GLOBCOVER land surface type classification, is proposed. The algorithm combines this land cover classification with remote sensing information on the vegetation cover fraction to obtain land surface emissivity maps for AATSR split-window bands. The emissivity estimates have been compared with ground measurements in two validation cases in the area of rice fields of Valencia, Spain, and they have also been compared to the classification-based emissivity product provided by MODIS (MOD11_L2). The results show that the error in emissivity of the proposed methodology is of the order of ±0.01 for most of the land surface classes considered, which will contribute to improve the operational land surface temperature measurements provided by the AATSR instrument.

KEYWORDS: land surface temperature, land surface emissivity, vegetation cover, AATSR, Globcover.

1. INTRODUCTION

The remote sensing measurement of land surface temperature (LST) using thermal infrared (TIR) data provided by instruments placed in satellites provides a monitoring of this magnitude on a synoptic, continuous and regular basis. The analysis of its evolution in time and space is a critical factor in many research fields such as weather forecasting, detection and monitoring of forest fires, natural hazards, climate change watch, energy fluxes estimation, etc. (Lentile et al. 2006, Zukhov et al. 2006, Tralli et al. 2005, Jin and Liang 2006, Anderson et al. 2008, Liang et al. 2010).

The main problem of measuring LST from remote sensing instruments is the need to correct the effects of the atmosphere in the measured signal and the knowledge of land surface emissivity (LSE). The atmospheric correction can be addressed with the use of radiative transfer models (RTM) with a description of the atmospheric temperature and humidity distributions (Cristóbal et al. 2009, Coll et al. 2010, Coll et al. 2012a, Zhou et al. 2012), or by means of multichannel (split-window) or multiangle (dual-angle) algorithms (Coll et al. 2006, Sòria and Sobrino 2007, Yu et al. 2008). In any of these cases, an independent estimation of LSE is needed, since these algorithms usually (but not always) show an explicit dependence on it.

Different methodologies have been developed to produce emissivity maps of the surface: emissivity-temperature separation algorithms such as TES (Gillespie et al. 1998) or TISI (Li and Becker 1993), multitemporal methods (Watson 1992, Wan and Li 1997), or algorithms based on physical models of the surface and estimations of fractional vegetation cover through spectral indices (Valor and Caselles 1996). The algorithms based on vegetation indices provide a practical way to estimate LSE with an acceptable accuracy (around 1% to 2% of error) at the typical split-window channels, as is the case of the Advanced Along-Track Scanning Radiometer (AATSR) instrument onboard the Envisat platform, and for those instruments that only have one TIR channel (e.g. Landsat-Thematic Mapper).

In this work, a procedure is presented to produce LSE maps based on the algorithm proposed by Valor and Caselles (1996), the so-called vegetation cover method (VCM), combined with the GLOBCOVER land surface classification (Arino et al. 2008), and a dynamic estimation of vegetation fraction from AATSR visible and near infrared bands. The proposed method is similar to some extent to the algorithm for LSE estimation used by the LST product of Terra-MODIS (Snyder et al. 1998), and for LSE estimations in Meteosat-SEVIRI (Peres and DaCamara 2005; Trigo et al. 2008). Although this methodology can be applied to any TIR sensor, in the present paper it is specifically applied to the AATSR instrument, since at present no LSE maps at 1-km spatial resolution are available for that sensor.

Initially, the algorithm has been applied at European scale, although it will be used to produce global LSE maps in the near future. This procedure will contribute to the improvement of LST estimates from AATSR data, since the current operational algorithm (Noyes et al. 2007) has been recognized to fail in some cases (with errors in the range 2-5 K) due to the use of surface classification and vegetation cover static maps at an spatial resolution of 0.5º x 0.5º, which is insufficient to cope with real surface heterogeneity in most cases (Coll et al. 2006, Coll et al. 2009, Noyes et al. 2007).

The paper proceeds as follows. First, the developed algorithm is presented in detail. In the results section a sensitivity analysis is performed for the LSE of all considered classes, and monthly mean emissivity maps for AATSR over Europe on 2007 are presented and analyzed. Finally, the main conclusions arising from this work are given.

2. METHODOLOGY

The LSE is calculated using the vegetation cover method (Valor and Caselles 1996), which is based on the geometric model proposed by Caselles and Sobrino (1989). The model defines the effective emissivity for a rough and heterogeneous surface from its component emissivities, and from an estimation of the fractional vegetation cover. In this method, the emissivity in band k is estimated through the relationship:

$$\varepsilon_k = \varepsilon_{kv}\, f + \varepsilon_{kg}\, (1\text{-}f) + 4 \langle d\varepsilon_k \rangle\, f\, (1\text{-}f) \qquad (1)$$

where ε_{kv} and ε_{kg} are the vegetation and ground emissivity, respectively, $\langle d\varepsilon_k \rangle$ is the maximum cavity term, and f is the fractional vegetation cover. The cavity term (the third term in the right-hand side of equation (1)) takes into account the effect of radiance internal reflections between the different components of a structured and rough surface (Caselles and Sobrino 1989).

The coefficients ε_{kv}, ε_{kg} and $\langle d\varepsilon_k \rangle$ depend on the surface type and spectral channel. To calculate them, it is first needed a classification of the surface to determine the vegetation and soil types and surface geometric structure found in a given area. Different operational classification schemes are available at present, among which we have considered the IGBP DISCover based on AVHRR data (Loveland et al. 2000), the MODIS Land Cover type product (Friedl et al. 2002; Friedl et al. 2010), the CORINE land cover based on Thematic Mapper data (Buttner et al. 2004), and the GLOBCOVER (GLC) dataset based on Medium Resolution Imaging Spectrometer (MERIS) data

(Bicheron et al., 2008; Arino et al. 2008). They have been compared in terms of classification accuracy in several areas and different contexts (Herold et al. 2008; See and Fritz 2006; Jung et al. 2006; Neumann et al. 2007; Heiskanen 2008; Wu et al. 2008), concluding that the key factor to assure classification accuracy is a good spatial resolution (Herold et al., 2008; Heiskanen, 2008). For this reason, the GLC dataset was selected since it shows the best combination of spatial (300 m) and spectral resolution presently. It is generated from Envisat-MERIS data, with reasonably good spectral resolution, using an unsupervised classification regional expert-tuned procedure similar to the predecessor GLC2000 classification (Bartholomé and Belward 2005), and is compatible with the standardized legend of the United Nations Food and Agriculture Organization Land Cover Classification System (LCCS, Di Gregorio and Jansen 2000). The GLC dataset was used to derive the surface type maps needed to set the emissivity coefficients of equation (1).

The initial 22 classes provided by the regional Western Europe GLC dataset were grouped and reduced to only 10 classes taking into account the components (soil and vegetation; bare rock; water, snow or ice; manmade construction materials, etc.) included in each class and the similarity between surface geometric structures. For the case of vegetated surfaces, the classes were grouped attending to structure (low grasses/crops, shrubs/trees lower than 5 m, shrubs/trees higher than 5 m), background surface (soil or water depending on flooding conditions), and vegetation type (green grasses, evergreen or deciduous shrubs/trees). All the classes corresponding to bare surfaces were also grouped into a single one, and the classes for urban areas, water, and snow and ice were maintained separately. Table 1 shows the resulting emissivity classes and the original

GLC surface types. The two first emissivity classes include those areas that are flooded or heavily irrigated most of the year, having water as surface background, with low (class 1) or high (class 2) vegetation, and with different fractional vegetation cover. Classes 3 and 4 contain areas with vegetation of low and medium height and dry soil as background. Classes 5 and 6 refer to forested areas with mainly deciduous or evergreen vegetation, respectively. Class 7 is regarded to urban built areas, and class 8 to bare surfaces (deserts, rocks, gravels, etc.). These bare surfaces, dominant in arid and semi-arid regions, may have the widest range of emissivity values, and thus may have a significant impact on emissivity estimation and on LST retrievals if one single value is used for them. Although these areas represent less than 1% of the pixels over Europe, additional efforts will be needed in future versions of the algorithm to distinguish between different bare surfaces, and thus to assign more adequate emissivity values in each case. Finally, classes 9 and 10 are related to water bodies, and areas permanently covered by snow and ice.

A set of coefficients ε_{kv}, ε_{kg} and $\langle d\varepsilon_k \rangle$ were derived for each of the emissivity classes established in Table 1, using the spectra included in the Advanced Spaceborne Thermal Emission and Reflection Radiometer (ASTER) Spectral Library (Baldridge et al. 2009), which is the most extensive published dataset of TIR reflectance spectra including both natural (soils, rocks, vegetation, minerals) and manmade (asphalt, tar, concrete, brick, tile) materials to date. Table 2 gives the values of these coefficients for equation (1) in the case of vegetated areas (classes 1 to 6), or alternatively average single-value emissivities in the case of non-vegetated surfaces (classes 7 to 10 corresponding to urban, bare rock, water, snow and ice). In all cases the used spectra were first convolved with the AATSR spectral response curves for bands at 11 and 12 μm to get the channel emissivity values.

For the case of vegetated surfaces (classes 1 to 6), the emissivity values for vegetation and ground (or water) were calculated using the samples given in the ASTER Spectral Library. These values were then averaged for the selected samples. In the case of soils, all available samples in the library (52) were used, which showed low variability in these bands (standard deviation smaller than ±0.005). There are only four vegetation samples**.** For classes 1 and 3, the green grass sample was used, for classes 2 and 4, the average between conifer and deciduous samples, for class 6 the conifer sample, and for class 5 the deciduous sample; the considered values for each class are in agreement, within the error, with measurements of complete plants for similar vegetation samples (Rubio et al. 2003). Rocks were excluded since they should not be usual in these surface types.

The classes showing low vegetation (1 and 3) were assigned a maximum cavity term $\langle d\varepsilon_k \rangle = 0$, since they are almost flat and show no cavities. For vegetated surfaces with a significant structure (emissivity classes 2, 4, 5 and 6) the maximum cavity term was determined with a simulation procedure. According to Caselles and Sobrino (1989), the cavity term for near nadir observation is given by

$$d\varepsilon_k = (1-\varepsilon_{kg})\, \varepsilon_{kv}\, F\, (1-f) \qquad (2)$$

where F is a shape factor that depends on the height (H) and separation (S) between the surface elements, and considers the energy transmission between them,

$$F = \left(1+\frac{H}{S}\right) - \sqrt{1+\left(\frac{H}{S}\right)^2}. \qquad (3)$$

The $d\varepsilon_k$ term was simplified and parameterized in terms of fractional vegetation cover only, and a maximum cavity term was calculated ($\langle d\varepsilon_k \rangle$ in equation (1)), which represents the maximum value that it can take for a given surface geometry with the fractional cover ranging from 0 to 1 (Valor and Caselles 1996); the resulting simplified expression is the third term in the right-hand side of equation (1). The maximum cavity term was calculated using equation (2) with the following procedure. First, for a given class reasonable values for the height (H) and size (L) of the vegetation elements were assigned taking into account the vegetation description given by the GLC dataset. In particular, for classes 2 and 4 (shrubs/trees lower than 5 m) values of H=(3±1) m and L=(3±1) m were taken; and for classes 5 and 6 (shrubs/trees higher than 5 m) values of H=(15±5) m and L=(5±2) m were considered, as mean values and standard deviations for each structure parameter. Secondly, for the vegetation fraction ranging from 0 to 1, the separation S and shape factor F were calculated for each f value, and then the cavity term given by equation (2) was calculated using the vegetation and ground/water emissivities described above. Finally, the maximum value of the cavity term was selected. The variability in the emissivity coefficients and in the structural parameters (height and size) were taken into account considering the vegetation and ground emissivities, and height and size of vegetation elements, as random variables following a Gaussian distribution with mean values and standard deviations given in table 2 (for emissivities) and above (for structural parameters). In consequence, the maximum value of the cavity term was calculated with this random procedure in 80 different simulations, and the average value and the standard deviation of the 80 results obtained were assigned to the value of the maximum cavity term given in table 2.

For the non-vegetated surfaces, average values were calculated from the samples provided by the ASTER Spectral Library. In the case of bare rock, 389 rock samples were averaged; 2 samples for water (sea and tap water), and 4 for snow and ice (fine, medium and coarse granular snow, and ice), giving unique effective values for each AATSR band. Certainly, rock emissivities show high standard deviations, and probably it would be necessary to distinguish them using additional rock maps in the future. In any case, the percentage of rock-exposed surfaces is relatively small in the GLC database for the area considered in this work, only 0.85% of pixels.

Finally, effective emissivity values were calculated for urban areas using the spectra for manmade materials: tiles and rubber were considered for roof emissivities, concrete for walls, and asphalt for paving. The effective emissivity was calculated adapting the model of Caselles and Sobrino (1989) to this kind of surfaces for near-nadir observation conditions:

$$\varepsilon_k = \varepsilon_{kr} P_r + \varepsilon_{kp} (1-P_r) + (1-\varepsilon_{kp}) \varepsilon_{kw} F (1-P_r) \quad (4)$$

where ε_{kr}, ε_{kp} and ε_{kw} are roof, paving and wall emissivities, P_r is the percentage of observed roofs, and F is the shape factor described above that depends on height and separation of buildings. The percentage of observed roofs was ranged from 0.2 (areas with wide streets and dispersed buildings, in which roofs occupy 20% of the surface) to 0.8 (areas with narrow streets and a high concentration of buildings close to each other, in which roofs occupy 80% of the observed surface). The shape factor in turn was changed from 0.5 (low height buildings in wide avenue areas) to 10 (very high buildings in narrow street areas).

Fractional vegetation cover (f) required in equation (1) was calculated from normalized difference vegetation index (NDVI) and reflectance values in AATSR red (0.659 μm) and near infrared (0.865 μm) bands using the relationship proposed by Valor and Caselles (1996). This relationship was derived using a linear mixture model with two components (soil and vegetation) that defines the channel reflectance of a mixed pixel as a combination of the soil and vegetation reflectance weighted by the fractional vegetation cover. Using this definition the fractional vegetation cover can be written in terms of NDVI as (Valor and Caselles 1996):

$$f = \frac{\left(1 - \frac{NDVI}{NDVI_s}\right)}{\left(1 - \frac{NDVI}{NDVI_s}\right) - K\left(1 - \frac{NDVI}{NDVI_v}\right)} \tag{5}$$

where NDVI is the pixel vegetation index, $NDVI_s$ and $NDVI_v$ are the index values for bare soil and full vegetation, and factor K is

$$K = \frac{\rho_{NIRv} - \rho_{Rv}}{\rho_{NIRs} - \rho_{Rs}} \tag{6}$$

where ρ_{Rv} and ρ_{NIRv} are respectively the red and near infrared reflectance values over full vegetation, and ρ_{Rs} and ρ_{NIRs} are the corresponding reflectances over bare soil. All these coefficients can be extracted from the AATSR scene itself, searching for the maximum and minimum NDVI values over the scene.

The described procedure was implemented in software that uses as inputs AATSR channels at 0.659 μm and 0.865 μm, the land cover classification GLC, and the emissivity coefficients by class given in table 2. The system obtains the coordinates of a given pixel and the measured values at each AATSR channel. The GLC map is used simultaneously to obtain the ground type of the pixel given by the coordinates of the AATSR scene. Since GLC data have a spatial resolution of 300 m, while AATSR data have a 1 km resolution, the system uses an interpolation by proportion of occupied areas algorithm (see Figure 1), to be able to combine them accurately, based on the geographical coordinates of both data sets.

This interpolation algorithm obtains the different types of vegetation and soil that form each AATSR pixel and estimates the proportion of the area that each vegetation and soil type represents. All 300m pixels within or partially overlapping the coarser 1km pixels are first identified, along with their respective land cover classes. Subsequently, the exact area of each GLC pixel overlapped by the AATSR pixel is calculated, based on their geographical coordinates and spatial resolutions. Therefore, the algorithm is able to estimate the values that need to be applied to the coefficients of equation (1). Each one is calculated as the weighted average of the values for that coefficient, related to all the emissivity classes involved. Thereby, the influence of each emissivity class is determined by the percentage that its area represents in the total area occupied by the AATSR pixel. The use of these weighted average coefficients for the vegetation and ground emissivities will minimize the error of estimate in emissivity, since this procedure accounts for the heterogeneity within each AATSR 1km pixel that is captured by the higher spatial resolution of GLC. The error of the interpolation method is lower than 1%, which is the error of the VCM model used to obtain the emissivity (see subsection 3.1 below). Therefore, the error derived from interpolating the GLC pixels with the AATSR ones is not significant compared to the error of the model.

The whole processing algorithm is summarized in the flowchart shown in Figure 2. First, the NDVI is calculated for all non-cloudy pixels on a daily basis, using the cloud mask provided by the AATSR product. Then, a procedure is started to search for the maximum and minimum NDVI values of the scene, and their respective reflectances, needed in equations (5) and (6) to calculate the fractional vegetation cover. In this procedure all pixels classified as bare rock, urban, water, snow or ice surfaces by GLC are excluded. For the surfaces classified as natural vegetation, the system checks that the surface is not accidentally covered by water, snow or ice, which can be the case mostly in winter scenes. In the case of water a threshold is used for the vegetation index values: if $NDVI<-0.10$ then the pixel is considered water, taking into account that usually the reflectance over water is smaller in the near infrared than in the red channels.

To detect snow- or ice-covered surfaces, an algorithm based on the MODIS snow-cover mapping procedure was used, which combines the reflectance in AATSR near infrared channel (0.865 μm) and the Normalized Difference Snow Index (NDSI) calculated as (Riggs et al. 2000; Hall et al. 2002):

$$NDSI = \frac{\rho_G - \rho_{SWIR}}{\rho_G + \rho_{SWIR}} \tag{7}$$

where ρ_G and ρ_{SWIR} are the reflectances in AATSR green (0.555 μm) and short-wave infrared (1.6 μm) channels, respectively. If NDSI is higher than 0.4, and reflectance in the near infrared band is larger than 0.11, then the surface is ice- or snow-covered (Hall et al. 2002). However, if the green band reflectance is lower than 0.10, then the pixel will not be ascribed as snow even if the other conditions are fulfilled, preventing pixels with very dark targets from being erroneously mapped as snow. All pixels identified as water or snow with these procedures, are later assigned the corresponding emissivity values given in table 2.

Once cloudy, snow- or water-covered pixels have been identified, the system produces a histogram of NDVI with the remaining pixels over the scene. The minimum and maximum NDVI values (for bare soil and vegetation) needed in equation (5) are selected as the values located at the 5^{th} and 95^{th} percentiles of the distribution, respectively, to assure that the selected values are representative of the whole scene and are not spurious values. For these minimum and maximum NDVI thresholds, the corresponding reflectances in the red and near infrared bands are collected to calculate the K factor in equation (6). Once the thresholds are established, the software calculates the fractional vegetation cover for vegetated surfaces, selects the emissivity coefficients depending on the GLC class from Table 2, and calculates effective emissivity with equation (1), or alternatively assigns directly the effective emissivity for non-vegetated surfaces. In this step, it is checked for the two first classes (flooded areas) if they are actually flooded or not, in order to select the adequate ε_g value (water or soil).

This procedure is followed for all available daily scenes within each month, allowing the processing of all respective orbits and dates, from which daily emissivity maps are produced. Then, a monthly composite is produced for each orbit by calculating the average, maximum and minimum valid emissivity values at each pixel over the month. Finally, the different orbits are merged to produce the final monthly emissivity map for Europe.

In order to minimize the impact of missing values of monthly emissivity on the retrieval of LST, a backup procedure is followed by the system to reduce the number of non-processed LST pixels. First, in order to estimate the minimum number of valid AATSR observations per month needed for the production of reliable emissivity estimates, the standard deviation of daily emissivities within a month were calculated to check what the variability in terms of emissivity is. The results showed that the monthly variability in emissivity is of the order of 0.004±0.002 in average on the whole scene, which is lower than the emissivity error of estimate given in the sensitivity analysis (see subsection 3.1). With this low variability, one single observation in a month can be a good approximation to an estimate of the monthly emissivity of a given pixel. If no observation is available in a given month, then the second approximation is to interpolate the emissivity value in that month by using the emissivity values corresponding to the previous month and the following month, respectively. Finally, for pixels that are covered by clouds most of the year, the third approach to the problem is the use of climatological averages to estimate a monthly value of NDVI, from which to calculate the monthly emissivity as described above.

3. RESULTS AND DISCUSSION

3.1. Sensitivity analysis

An error analysis of the emissivities calculated with the described methodology was conducted using error propagation theory. Following equation (1), the error in emissivity is given by:

$$\delta\varepsilon = f\,\delta\varepsilon_v + (1-f)\,\delta\varepsilon_g + 4\,f(1-f)\,\delta < d\varepsilon > + \lfloor \varepsilon_v - \varepsilon_g + 4 < \varepsilon > (1-2f) \rfloor \delta f \qquad (8)$$

where $\delta\varepsilon_v$, $\delta\varepsilon_g$ and $\delta < d\varepsilon >$ are the errors in the emissivity coefficients of equation (1), which are given in table 2, and δf is the error in the vegetation fraction. Methods that retrieve fractional vegetation cover from NDVI using linear relationships provide f with errors ranging from ±0.04 to ±0.20 (Gutman and Ignatov 1998, Zeng et al. 2000, Xiao and Moody 2005, Jiang et al. 2006, Zhou et al. 2009, Verger et al. 2009). The algorithm proposed in the present paper (Eq. (5)) uses a linear relationship between vegetation cover and reflectance, which implies a non-linear relationship between f and NDVI, capturing the non-linearity actually observed, especially at high values of vegetation fraction (for which NDVI usually saturates). For this kind of non-linear algorithms errors of ±0.08 in the fractional vegetation cover retrieval have been reported (Purevdorj et al. 1998). In particular, Jiang et al. (2006) analyzed the performance of a non-linear algorithm based on linear relationships between reflectance and fractional vegetation cover (the so-called Scaled Difference Vegetation Index, SDVI) equivalent to the methodology here proposed, and found that it was able to provide f with an uncertainty of ±0.07 in a validation exercise. In consequence, a value of ±0.15 in δf has been used to address the sensitivity analysis, which is twice the error values reported for that type of algorithm, and is of the same order of magnitude than the higher errors observed in linear algorithms.

Table 3 shows the average, maximum, minimum and standard deviation of the errors in emissivity for f values raging from 0 to 1 in each class corresponding to vegetated areas, and the average error calculated for non-vegetated zones. The lowest errors correspond to flooded areas (classes 1 and 2 with water at the background), croplands/grasslands (class 3), and urban, water and snow/ice areas (classes 7, 9 and 10) with values from ±0.001 to ±0.008, which would result in LST errors from ±0.1 to ±0.6 K (Galve et al. 2008). The largest error in emissivity is found in the bare rock case (class 8) with a value of ±0.05, due to the high variability of this kind of surfaces, which would produce an LST error around ±4 K. Although these areas occupy a small fraction of the total surface considered, it would be desirable to use rock maps in the future to refine the methodology in those areas. The remaining classes (4, 5 and 6) show errors in emissivity around ±0.014 that would correspond to LST errors of about ±1 K.

3.2. Emissivity product for AATSR

Monthly emissivity maps of Europe were produced with the proposed procedure for year 2007, using all available AATSR images for each month, processing a total of 2,257 scenes in the whole year. Figure 3 shows the monthly fractional vegetation cover for each month calculated as the average value of each valid pixel within each month. It is observed a variation of vegetation cover in Europe during the year with peaks in spring and autumn, and lower vegetation fractions in summer and especially in winter. The low coverage in some mountainous areas such as the Scandinavian Peninsula, the Alps or the Pyrenean Mountains in winter months, is due to the presence of snow and water. Figure 4 presents the monthly emissivity for band AATSR-11 μm; the emissivity variation in each month (difference between maximum and minimum emissivity value in a pixel basis, not shown) was calculated resulting in negligible values for most pixels, giving confidence in the stability of the proposed method.

To test the consistency of the methodology, the time evolution of fractional vegetation cover and emissivity was checked for the emissivity classes defined in Table 1, selecting adequate locations for each case. Figure 5 shows the results. For class 1 the area of rice fields in the Albufera of Valencia, Spain (39º 15' N, 0º 18' W) was used. In this case the vegetation cover follows the typical phenology of rice plants, which are seeded in May and harvested in September, the fields being completely flooded during this period until January; then the fields are dried, showing scarce and low grasses (January to April), until a new annual period begins. Consequently, emissivity is low in April, increases from May to July (when the vegetation cover is highest), decreases to September (when it is harvested) and peaks again in October and November due to flooded fields without vegetation. For class 3 a cropland area placed near Fondouce, France (46° 4' N, 0° 53' W) was selected. In this case the vegetation cover starts from a relatively low value in January, increasing until reaching a maximum value in June and decreasing gradually until January; the emissivity follows the same tendency as vegetation cover does. In class 4 a shrubland area near Tilj, Croatia (43° 36' N 16° 46' E) was used, showing an irregular variation for vegetation cover during the year and an emissivity with relatively low variability (the values on December are due to the presence of snow). An area in Montebruno, Italy (44º 31' N, 9º 15' E) was selected as an example of broadleaved/needleleaved deciduous forest (class 5). The vegetation fractional cover typically increases during the year peaking in summer and decreasing in autumn; since emissivity for the soil (0.970) and the vegetation (0.973) are similar, the effective emissivity is lower both for low and high vegetation cover fractions, and it is higher at intermediate fractions due to cavity effects, which explain the peak values in spring. In case of class 6, broadleaved/needleleaved evergreen forest, a site located in Moray, Scotland (57° 23' N, 3° 49' W) was analyzed showing low variation both in fractional vegetation cover and emissivities. There were no well-defined areas in the scene for class 2 (flooded forest/shrubland), and the remaining classes (7 through 10) exhibit constant values with time as expected, since they do not depend on vegetation cover (urban area, bare rock, water, snow and ice).

3.3. Validation

A validation exercise was conducted comparing the emissivity values produced by the system with concurrent ground measurements carried out in the area of rice fields placed in the Albufera of Valencia, Spain (Coll et al. 2007), during two different moments of the year (see Figure 5, class 1). First, it was compared the emissivity value when the surface is fully covered of rice with water as background (July). In channel AATSR-11 μm the measured emissivity in the field was 0.985±0.002 and the system value was 0.982±0.001, with a difference of +0.003, whereas for AATSR-12 μm band the measured emissivity was 0.980±0.005 and the system value was 0.988±0.002, showing a difference of -0.008. Secondly, the comparison was conducted on April, when the rice fields are fallow and in dry conditions (Coll et al. 2012b); in this case the measured emissivity in the field was 0.957±0.005 (Mira et al. 2007) in channel AATSR-11 μm and the system value was 0.970±0.001, with a difference of -0.013, whereas for AATSR-12 μm band the measured emissivity was 0.954±0.005 and the system value was 0.977±0.001, showing a difference of -0.023. The validation results are within ±0.010, except for the case of bare soil in channel AATSR-12 μm. This shows a reasonably good result, although the validation exercise is very limited in space and time. Nevertheless, the coefficients used for dry bare soils, calculated from all the soil sample spectra of the ASTER library (which showed a low dispersion, see Table 2), will be revised using additional datasets in order to reduce the larger difference observed in channel AATSR-12 μm.

3.4. Comparison with MODIS emissivity product

A comparison of the AATSR emissivity maps with other similar land surface emissivity products (designed for use in typical split-window channels, and based on a land cover classification) was carried out in order to analyze spatial and temporal patterns. The MODIS classification-based emissivity product (Snyder et al. 1998) was considered taking into account its similarity to the methodology proposed in the present paper. Although the LST product provided by SEVIRI also uses a classification-based emissivity estimate (Peres and DaCamara 2005, Trigo et al. 2008), it is an internal product that was not available to perform the comparison.

The selected product is the MODIS/Terra level-2 LST/E data (MOD11_L2), which provides LST measurements using the generalized split-window algorithm (Wan and Dozier, 1996). For this algorithm, emissivity estimates in MODIS split-window bands 31 and 32 are needed, which are calculated using the classification-based emissivity method (Snyder et al. 1998) and included also as data in the MOD11_L2 product. This method uses as input the MODIS land cover product (MOD12Q1) provided yearly, and assigns to each class emissivity values that were estimated using kernel models and considering the spectral and structural characteristics of each surface type (Snyder and Wan 1998). The algorithm also includes dynamical and seasonal factors, such as the use of the snow cover product (MOD10_L2) to check the presence of occasional water, snow or ice in an area, or the use of the vegetation index product (MOD13_VI) to determine the greenness of senescent vegetation. Presently, three different versions of this product (V4, V41 and V5) are available; for the comparison, the V41 was chosen because it addresses underestimation problems in the V5 Climate Modeling Grid (CMG) products, and the production date for this collection starts with MODIS/Terra data acquisition from January 2007.

In order to do the comparison, equivalent MOD11_L2 composite maps over Europe were produced monthly by averaging the data provided by the MOD11A2 product on an eight-day basis using a sinusoidal projection. After the MOD11_L2 monthly maps were generated, emissivity differences were calculated in a pixel-by-pixel basis (MODIS LSE minus AATSR LSE) for the two split-window channels. Figure 6 shows the emissivity difference maps for January, April, July and October, Figure 7 presents the histograms of the difference data for the same months, and Table 4 gives the summary statistics for the results.

Most of the observed differences are within ±0.01 in emissivity, with average values for the whole scene around zero in all seasons, below the expected error of estimate described in the sensitivity analysis subsection. The temporal comparison shows that in January MODIS emissivities are +0.01 larger than AATSR emissivities in most places and for the two channels (this bias is larger for channel at 12 μm), except in northern Europe. For the other seasons this bias is significantly reduced. The spatial patterns of the difference maps show that the larger disparity between both products is grouped geographically. The majority of the differences between +0.01 and +0.02 are located in southern Europe (Portugal, Spain, and Italy). Oppositely, the differences lower than -0.02 are located in Scandinavia, and other high-altitude places such as the Alps, where the presence of water and snow is more common. Thus, the proposed method is providing higher emissivity values for places where snow and water are present, and lower emissivity values in arid and semi-arid areas. These differences can be due to several reasons: (i) the different land cover classification used in each case, the yearly MOD12Q1 product in MODIS that can be more dynamic, and GLOBCOVER in AATSR that is a static classification; (ii) the different emissivity coefficients used for each surface type, especially for bare soil and rocky areas (these are higher in the MODIS case, which could explain higher emissivity values in arid areas); (iii) the calculation of the effective emissivity in case of AATSR is dynamic for vegetated surfaces since it is based on the calculation of fractional vegetation cover from NDVI, while it is semi-static in MODIS since this product does not estimate fractional vegetation covers, only estimates the phenological state from vegetation index data and time of the year. Despite these differences, the two products seem to be quite consistent, at least in relation to the expected error of estimate in emissivity.

4. SUMMARY AND CONCLUSIONS

In this work a methodology for automatic generation of LSE maps is proposed that was developed taking as starting point the Vegetation Cover Method (Valor and Caselles 1996). The new algorithm is based on the combination of VCM with a classification of the land surface (GLOBCOVER), which allows: (i) considering all surfaces, not only natural land surfaces related to vegetation cover, but also urban, water or snow areas, for instance; and (ii) adjusting the emissivity coefficients of the algorithm depending on the different surface components and geometries, instead of using general coefficients globally, reducing thus the error of estimate in LSE. In addition, the algorithm uses a dynamic estimation of the fractional vegetation cover through the year that allows capturing LSE variations due to changes at surface level, including the occasional presence of water or snow.

The sensitivity analysis of the methodology shows that in most cases LSE can be achieved with errors of the order of ±1% or lower, which implies errors in LST lower than ±1 K, except for the case of bare areas for which additional efforts will be needed (including geologic/rock maps if available, or using a complementary methodology). These results have been confirmed by a validation exercise comparing the LSE produced by the algorithm to ground reference emissivity measurements conducted in rice fields in the Albufera of Valencia, Spain, in two times of the year. However, the validation has indicated that the selected emissivity value for dry bare soil should be revised considering additional published datasets, especially for channel AATSR-12 μm.

The proposed LSE maps for AATSR have been also compared to the equivalent MODIS product (MOD11_L2) in the year 2007. The comparison resulted in emissivity differences mostly within ±0.01 with average values for the whole scene around zero in all seasons, below the expected error of estimate given by the sensitivity analysis. The highest differences between products were observed temporally in January, and spatially in southern Europe and Scandinavia.

The proposed methodology can be adapted to different present and future TIR remote sensors, but in this work it has been applied to AATSR data over Europe, since it has been recognized the need of improvement in the LST operational product, in particular using classification schemes with better spatial resolution. In fact, the methodology here presented is part of an effort to improve AATSR LST estimations through the use of a split-window algorithm with explicit dependence on emissivity (Coll et al. 2012b). Further developments will include the improvement of LSE estimation over bare areas, the production of global LST maps based on AATSR data with the proposed LSE methodology, and also the adaptation to present and new TIR sensors.

ACKNOWLEDGMENTS

This work was funded by the Generalitat Valenciana (project PROMETEO/2009/086, and contract of Eduardo Caselles) and the Spanish *Ministerio de Ciencia e Innovación* (projects CGL2007-64666/CLI, CGL2010-17577/CLI and CGL2007-29819-E, co-financed with FEDER funds). AATSR data were provided by European Space Agency (ESA) under Cat-1 project 3466. We also thank ESA and the ESA GLOBCOVER Project, led by MEDIAS-France, for the GLOBCOVER classification data. The comments and suggestions of three anonymous reviewers that improved the paper are also acknowledged.

REFERENCES

Anderson, M.C., Norman, J.M., Kustas, W.P., Houborg, R., Starks, P.J. and Agam, N. (2008). A thermal-based remote sensing technique for routine mapping of land-surface carbon, water and energy fluxes from field to regional scales. *Remote Sensing of Environment*, 12: 4227-4241.

Arino, O., Bicheron, P., Achard, F., Latham, J., Witt, R. and Weber, J.L. (2008). "GlobCover: the most detailed portrait of Earth", ESA Bulletin 136, European Space Agency.

Baldridge, A. M., Hook, S. J., Grove, C. I. and Rivera, G. (2009). The ASTER Spectral Library Version 2.0. *Remote Sensing of Environment*, 113: 711–715.

Bartholomé, E. and Belward, A.S. (2005). GLC2000: a new approach to global land cover mapping from Earth observation data. *International Journal of Remote Sensing*, 26(9): 1959-1977.

Bicheron, P., Huc, M., Henry, C., Bontemps, S. and Lacaux, J.P. (2008). Globcover: Products Description Manual. Issue 2, Rev. 2, http://ionia1.esrin.esa.int/images/GLOBCOVER_Product_Specification_v2.pdf.

Buttner, G., Feranec, J., Jaffrain, G., Mari, L., Maucha, G. and Soukup, T. (2004). The European Corine Land Cover 2000 Project. *XX Congress of International Society for Photogrammetry and Remote Sensing*. Istanbul, Turkey.

Caselles, V., and Sobrino, J.A. (1989). Determination of frosts in orange groves from NOAA-9 AVHRR data. *Remote Sensing of Environment, 29:* 135-146.

Coll, C., Caselles, V., Galve, J.M., Valor, E., Niclòs, R. and Sánchez, J.M. (2006). Evaluation of split-window and dual-angle correction methods for land surface temperature retrieval from Envisat/Advanced Along Track Scanning Radiometer (AATSR) data. *Journal of Geophysical Research*, 111, doi:10.1029/2005JD006830.

Coll, C., Caselles, V., Valor, E., Niclòs, R., Sánchez, J.M., Galve, J.M. and Mira, M. (2007). Temperature and emissivity separation from ASTER data for low spectral contrast surfaces. *Remote Sensing of Environment*, 110: 162-175.

Coll, C., Hook, S.J. and Galve, J.M. (2009). Land Surface Temperature from the Advanced Along-Track Scanning Radiometer: Validation Over Inland Waters and Vegetated Surfaces. *IEEE Transactions on Geoscience and Remote Sensing*, 47: 350-360.

Coll, C., Galve, J.M., Sánchez, J.M. and Caselles, V. (2010) . Validation of Landsat-7/ETM+ thermal-band calibration and atmospheric correction with ground-based measurements. *IEEE transactions on Geoscience and Remote Sensing*, 48 (1): 547-555.

Coll, C., Caselles, V., Valor, E. and Niclòs, R. (2012a). Comparison between different sources of atmospheric profiles for land surface temperature retrieval from single channel thermal infrared data. *Remote Sensing of Environment* 117: 199-210.

Coll, C., Valor, E., Galve, J.M., Mira, M., Bisquert, M., García-Santos, V., Caselles, E. and Caselles, V. (2012b). Long-term accuracy assessment of land surface temperatures derived from the Advanced Along-Track Scanning Radiometer. *Remote Sensing of Environment*, 116: 211-225.

Cristóbal, J., Jiménez-Muñoz, J.C., Sobrino, J.A., Ninyerola, M. and Pons, X. (2009). Improvements in land surface temperature retrieval from the Landsat series thermal band using water vapor and air temperature. *Journal of Geophysical Research* 114, doi 10.1029/2008JD010616.

Di Gregorio, A. and Jansen, L. (2000). *Land Cover Classification System (LCCS): Classification Concepts and User,* FAO Corporate Document Repository.

Friedl, M.A., McIver, D.,K., Hodges, J.C.F., Zhang, X.Y., Muchoney, D., Strahler, A.H., Woodcock, C.E., Gopal, S., Schneider, A., Cooper, A., Baccini, A., Gao, F. and Schaaf, C. (2002). Global land cover mapping from MODIS: algorithms and early results. *Remote Sensing of Environment* 83: 287-302.

Friedl, M.A., Sulla-Menashe, D., Tan, B., Schneider, A., Ramankutty, N., Sibley, A. and Huang, X. (2010). MODIS Collection 5 global land cover: algorithm refinements and characterization of new datasets. *Remote Sensing of Environment,* 114: 168-182.

Galve J.M., Coll, C., Caselles V. and Valor E. (2008). An atmospheric radiosounding database for generating Land Surface Temperature algorithms. *IEEE Transactions on Geosciences and Remote Sensing*, 46 (5): 1547-57.

Gillespie, A.R., Matsunaga, T., Rokugawa, S., and Hook, S. J. (1998). Temperature and emissivity separation from Advanced Spaceborne Thermal Emission and Reflection Radiometer (ASTER) images. *IEEE Transactions on Geoscience and Remote Sensing*, 36: 1113–1125.

Gutman, G. and Ignatov, A. (1998). The derivation of green vegetation fraction from NOAA/AVHRR data for use in numerical weather prediction models. *International Journal of Remote Sensing*, 19 (8): 1533-1543.

Hall, D. K., Riggs, G. A., Salomonson, V. V., DeGirolamo, N. E., Bayr, K. J., and Jin, J. M. (2002). MODIS Snow-cover products. *Remote Sensing of Environment*, 83: 181– 194.

Herold, M., Mayaux, P., Woodcock, C.E., Baccini, A., and Schmullius, C. (2008). Some challenges in global land cover mapping: An assessment of agreement and accuracy in existing 1 km datasets. *Remote Sensing of Environment*, 112: 2538–2556.

Heiskanen, J. (2008). Evaluation of global land cover data sets over the tundra-taiga transition zone in northernmost Finland. *International Journal of Remote Sensing*, 29(13): 3727-3751.

Jiang, ZY, Huete, AR, Chen, J, Chen, YH, Li, J, Yan, GJ, Zhang, XY (2006). Analysis of NDVI and scaled difference vegetation index retrievals of vegetation fraction. *Remote Sensing of Environment* 101: 366-378.

Jin, M. and Liang, S. (2006). An Improved Land Surface Emissivity Parameter for Land Surface Models Using Global Remote Sensing Observations. *Journal of Climate*, 19: 2867–2881.

Jung, M., Henkel, K., Herold, M. and Churkina, G. (2006). Exploiting synergies of global land cover products for carbon cycle modelling. *Remote Sensing of Environment*, 101: 534–553.

Lentile, L.B., Holden, Z.A., Smith, A.M.S., Falkowski, M.J., Hudak, A.T., Morgan, P., Lewis, S.A., Gessler, P.E., and Benson, N.C. (2006). Remote sensing techniques to assess active fire characteristics and post-fire effects. *International Journal of Wildland Fire* 15: 319–345.

Li, Z.-L., and Becker, F. (1993). Feasibility of land surface temperature and emissivity determination from AVHRR data. *Remote Sensing of Environment*, 43: 67-85.

Liang, S., Kustas, W., Schaepman-Strub, G., and Li, X. (2010). Impacts of climate change and land use change on land surface radiation and energy budgets. *IEEE Journal of Selected Topics in Earth Observations and Remote Sensing* 3: 219-224.

Loveland, T.R., Reed, B.C., Brown, J.F., Ohlen, D.O., Zhu, Z., Yang, L. and Merchant, J.W. (2000). Development of a global land cover characteristics database and IGBP DISCover from 1 km AVHRR data. *International Journal of Remote Sensing*, 21: 1303–1330.

Mira, M., Valor, E., Boluda, R., Caselles, V., and Coll, C. (2007). Influence of soil water content on the thermal infrared emissivity of bare soils: Implication for land surface temperature determination. *Journal of Geophysical Research* 112, doi: 10.1029/2007JF000749.

Neumann, K., Herold, M., Hartley, A. and Schmullius, C. (2007). Comparative assessment of CORINE2000 and GLC2000: Spatial analysis of land cover data for Europe. *International Journal of Applied Earth Observation and Geoinformation*, 9: 425–437.

Noyes, E., G. Corlett, J. Remedios, X. Kong, and D. Llewellyn-Jones (2007). An Accuracy Assessment of AATSR LST Data Using Empirical and Theoretical Methods. *Proceedings of the Envisat Symposium 2007*, Montreux, Switzerland, ESA SP-636.

Peres, L.F., and DaCamara, C.C. (2005). Emissivity maps to retrieve land-surface temperature from MSG/SEVIRI. *IEEE Transactions on Geoscience and Remote Sensing*, 43: 1834-1844.

Purevdorj, Ts., Tateishi, R., Ishiyama, T. and Honda, Y. (1998). Relationships between percent vegetation cover and vegetation indices. *International Journal of Remote Sensing* 19 (18): 3519-3535.

Riggs, G. A., Barton, J. S., Casey, K. A., Hall, D. K., and Salomonson, V. V. (2000). MODIS Snow Products Users' Guide. http://www.icess.ucsb.edu/modis/SnowUsrGuide/usrguide.html.

Rubio, E., Caselles, V., Coll, C., Valor, E., and Sospedra, F. (2003). Thermal-infrared emissivities of natural surfaces: improvements on the experimental set-up and new measurements. *International Journal of Remote Sensing* 24: 5379-5390.

See, L.M., and Fritz, S. (2006). A Method to Compare and Improve Land Cover Datasets: Application to the GLC-2000 and MODIS Land Cover Products. *IEEE Transactions on Geoscience and Remote Sensing* 44 (7): 1740-1746.

Snyder,W. C., and Wan Z. (1998). BRDF models to predict spectral reflectance and emissivity in the thermal infrared. *IEEE Transactions on Geoscience and Remote Sensing* 36: 214- 225.

Snyder, W.C., Wan, Z., Zhang, Y., and Feng, Y.Z. (1998). Classification-based emissivity for land surface temperature measurement from space. *International Journal of Remote Sensing* 19: 2753-2774.

Sòria, G. and Sobrino, J.A. (2007). ENVISAT/AATSR derived land surface temperature over a heterogeneous region. *Remote Sensing of Environment* 111: 409-422.

Tralli, D.M., Blom, R.G., Zlotnicki, V., Donnellan, A. and Evans, D.L. (2005). Satellite remote sensing of earthquake, volcano, flood, landslide and coastal inundation hazards. *ISPRS Journal of Photogrammetry and Remote Sensing*, 59: 185-198.

Trigo, I.F., Peres, L.F., DaCamara, C.C. and Freitas, S.C. (2008). Thermal land surface emissivity retrieved from SEVIRI/Meteosat. *IEEE Transactions on Geoscience and Remote Sensing* 46: 307-315.

Valor, E. and Caselles, V. (1996). Mapping Land Surface Emissivity from NDVI: application to European, African, and South American Areas. *Remote Sensing of Environment* 57: 167-184.

Verger, A., Martínez, B., Camacho-de Coca, F. and García-Haro, F.J. (2009). Accuracy assessment of fraction of vegetation cover and leaf area index estimates from pragmatic methods in a cropland area. *International Journal of Remote Sensing* 30 (10): 2685-2704.

Wan, Z. and Dozier, J. (1996). A generalized split-window algorithm for retrieving land-surface temperature from space. *IEEE Transactions on Geoscience and Remote Sensing* 34: 892-905.

Wan, Z., and Li, Z.-L. (1997). A physics-based algorithm for land-surface emissivity and temperature from EOS/MODIS data. *IEEE Transactions on Geoscience and Remote Sensing* 35: 980-996.

Watson, K. (1992). Two-temperature method for measuring emissivity. *Remote Sensing of Environment* 42: 117-121.

Wu, W., Shibasaki, R., Yang, P., Ongaro, L., Zhou, Q., and Tang, H. (2008). Validation and comparison of 1 km global land cover products in China. *International Journal of Remote Sensing* 29(13): 3769-3785.

Xiao, J. and Moody, A. (2005). A comparison of methods for estimating fractional green vegetation cover within a desert-to-upland transition zone in central New Mexico, USA. *Remote Sensing of Environment* 98: 237-250.

Yu, Y., Privette, J.L. and Pinheiro, A.C. (2008). Evaluation of Split-Window Land Surface Temperature Algorithms for Generating Climate Data Records. *IEEE Transactions on Geoscience and Remote Sensing* 46: 179-192.

Zeng, X., Dickinson, R.E., Walker, A., Shaikh, M., DeFries, R.S. and Qi, J. (2000). Derivation and evaluation of global 1-km fractional vegetation cover data for land modeling. *Journal of Applied Meteorology* 39: 826-839.

Zhou, X., Guan, H., Xie, H. and Wilson, J.L. (2009). Analysis and optimization of NDVI definitions and areal fraction models in remote sensing of vegetation. *International Journal of Remote Sensing* 33 (3): 721-751.

Zhou, J., Li, J., Zhang, L., Hu, D. and Zhan, W. (2012). Intercomparison of methods for estimating land surface temperature from a Landsat-5 TM image in an arid region with low water vapour in the atmosphere. *International Journal of Remote Sensing* 33: 2582–2602.

Zhukov, B., Lorenz, E., Oertel, D., Wooster, M.J., Roberts, G. (2006). Spaceborne detection and characterization of fires during the bi-spectral infrared detection (BIRD) experimental small satellite mission (2001–2004). *Remote Sensing of Environment* 100: 29–51.

Table 1. Emissivity classes by surface type, and their correspondence with the biomes defined by the GLOBCOVER (GLC) dataset (after Coll et al. 2012b). The percentage occurrence over Europe of each emissivity class is given in parentheses in the first column.

Emissivity class	**GLC Class**	**Description**
1. Flooded vegetation, crops and grasslands **(0.75%)**	11	Post-flooding or irrigated croplands (or aquatic)
	13	Post-flooding or irrigated herbaceous crops
	180	Closed to open (>15%) grassland or woody vegetation on regularly flooded or waterlogged soil - Fresh, brackish or saline water
	185	Closed to open (>15%) grassland on regularly flooded or waterlogged soil - Fresh or brackish water
2. Flooded forest and shrublands **(<0.01%)**	170	Closed (>40%) broadleaved forest or shrubland permanently flooded - Saline or brackish water
3. Croplands and grasslands **(19.69%)**	14	Rainfed croplands
	15	Rainfed herbaceous crops
	20	Mosaic cropland (50-70%) / vegetation (grassland/shrubland/forest) (20-50%)
	21	Mosaic cropland (50-70%) / grassland or shrubland (20-50%)
	120	Mosaic grassland (50-70%) / forest or shrubland (20-50%)
	140	Closed to open (>15%) herbaceous vegetation (grassland, savannas or lichens/mosses)
	141	Closed (>40%) grassland
	150	Sparse (<15%) vegetation
	151	Sparse (<15%) grassland
4. Shrublands **(3.24%)**	16	Rainfed shrub or tree crops (cash crops, vineyards, olive tree, orchards…)
	30	Mosaic vegetation (grassland/shrubland/forest) (50-70%) / cropland (20-50%)
	130	Closed to open (>15%) (broadleaved or needleleaved, evergreen or deciduous) shrubland (<5m)
	131	Closed to open (>15%) broadleaved or needleleaved evergreen shrubland (<5m)
	134	Closed to open (>15%) broadleaved deciduous shrubland (<5m)
	152	Sparse (<15%) shrubland
5. Broadleaved/ needleleaved deciduous forest **(10.37%)**	40	Closed to open (>15%) broadleaved evergreen or semi-deciduous forest (>5m)
	50	Closed (>40%) broadleaved deciduous forest (>5m)
	60	Open (15-40%) broadleaved deciduous forest/woodland (>5m)
	90	Open (15-40%) needleleaved deciduous or evergreen forest (>5m)
	91	Open (15-40%) needleleaved deciduous forest (>5m)
6. Broadleaved/ needleleaved evergreen forest **(6.46%)**	32	Mosaic forest (50-70%) / cropland (20-50%)
	70	Closed (>40%) needleleaved evergreen forest (>5m)
	92	Open (15-40%) needleleaved evergreen forest (>5m)
	100	Closed to open (>15%) mixed broadleaved and needleleaved forest (>5m)
	101	Closed (>40%) mixed broadleaved and needleleaved forest (>5m)
	110	Mosaic forest or shrubland (50-70%) / grassland (20-50%)
7. Urban area **(0.45%)**	190	Artificial surfaces and associated areas (Urban areas >50%)
8. Bare rock **(0.85%)**	200	Bare areas
	201	Consolidated bare areas (hardpans, gravels, bare rock, stones, boulders)
	202	Non-consolidated bare areas (sandy desert)
	203	Salt hardpans
9. Water **(57.2%)**	210	Water bodies
10. Snow and ice **(0.99%)**	220	Permanent snow and ice

Table 2. Emissivity classes with the values for the parameters of equation (1) in the AATSR-11 and AATSR-12 μm channels (after Coll et al. 2012b). In classes 1 and 2, (d) stands for a dry (non-flooded) surface with a soil as background, and (w) stands for a wet (flooded) surface.

Emissivity Class	**AATSR-11 μm**			**AATSR-12 μm**		
	ε_v	ε_g	**<dε>**	ε_v	ε_g	**<dε>**
1. Flooded vegetation/ crops/grasslands	0.983±0.005	0.970±0.005 (d) 0.991±0.001 (w)	0	0.989±0.005	0.977±0.004 (d) 0.985±0.001 (w)	0
2. Flooded forest/shrubland	0.981±0.008	0.970±0.005 (d) 0.991±0.001 (w)	0.014±0.004 (d) 0.004±0.001(w)	0.982±0.009	0.977±0.004 (d) 0.985±0.001 (w)	0.010±0.003 (d) 0.007±0.002 (w)
3. Croplands/grasslands	0.983±0.005	0.970±0.005	0	0.989±0.005	0.977±0.004	0
4. Shrublands	0.981±0.008	0.970±0.005	0.014±0.004	0.982±0.009	0.977±0.004	0.010±0.003
5. Broadleaved/needleleaved deciduous forest	0.973±0.005	0.970±0.005	0.019±0.006	0.973±0.005	0.977±0.004	0.015±0.004
6. Broadleaved/needleleaved evergreen forest	0.989±0.005	0.970±0.005	0.019±0.005	0.991±0.005	0.977±0.004	0.015±0.004
7. Urban area	0.980±0.005			0.986±0.005		
8. Bare rock	0.93±0.05			0.95±0.05		
9. Water	0.991±0.001			0.985±0.001		
10. Snow and ice	0.990±0.004			0.971±0.014		

Table 3. Errors in emissivity in the AATSR-11 and AATSR-12 μm channels for the different vegetated and non-vegetated classes. The average, standard deviation, maximum and minimum values of the errors when vegetation fraction ranges from 0 to 1, are presented. In classes 1 and 2, (d) stands for a dry (non-flooded) surface with a soil as background, and (w) stands for a wet (flooded) surface.

Emissivity Class	**AATSR-11 μm**				**AATSR-12 μm**			
	avg	**std dev**	**max**	**min**	**avg**	**std dev**	**max**	**min**
1. Flooded vegetation/ crops/grasslands	0.007 (d) 0.004 (w)	0.000 (d) 0.001 (w)	0.007(d) 0.006(w)	0.007 (d) 0.002 (w)	0.006 (d) 0.004 (w)	0.000 (d) 0.001 (w)	0.007 (d) 0.006 (w)	0.007 (d) 0.002 (w)
2. Flooded forest/shrubland	0.014 (d) 0.007 (w)	0.001 (d) 0.003 (w)	0.015 (d) 0.012 (w)	0.011 (d) 0.002 (w)	0.012 (d) 0.008 (w)	0.001 (d) 0.003 (w)	0.014 (d) 0.014 (w)	0.010 (d) 0.005 (w)
3. Croplands/grasslands	0.007	0.000	0.007	0.007	0.006	0.000	0.007	0.006
4. Shrublands	0.014	0.001	0.015	0.011	0.012	0.001	0.014	0.010
5. Broadleaved/needleleaved deciduous forest	0.015	0.002	0.017	0.011	0.012	0.002	0.015	0.009
6. Broadleaved/needleleaved evergreen forest	0.014	0.003	0.019	0.010	0.012	0.002	0.015	0.008
7. Urban area	0.005				0.005			
8. Bare rock	0.05				0.05			
9. Water	0.001				0.001			
10. Snow and ice	0.004				0.014			

Table 4.- Summary statistics of the emissivity difference images for the different seasons of the year 2007 in each channel (11 and 12 µm).

	Channel 11µm				**Channel 12µm**			
	January	April	July	October	January	April	July	October
Minimum	-0.03	-0.03	-0.03	-0.03	-0.02	-0.02	-0.03	-0.02
Maximum	0.02	0.02	0.02	0.02	0.02	0.02	0.02	0.02
Mean	0	0	0	0	0	0	0	0
Standard deviation	0.01	0.01	0.01	0.01	0.01	0	0.01	0.01

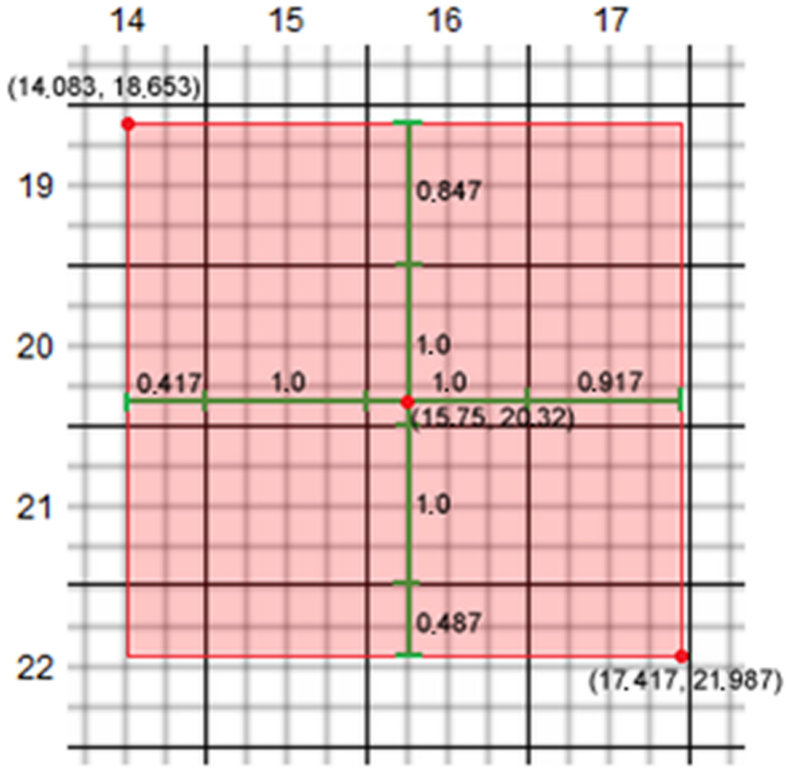

Figure 1.- Example of an AATSR pixel (1 km, shown in red), interpolated with GLC pixels (300 m, shown in black), according to the interpolation by proportion of occupied areas algorithm.

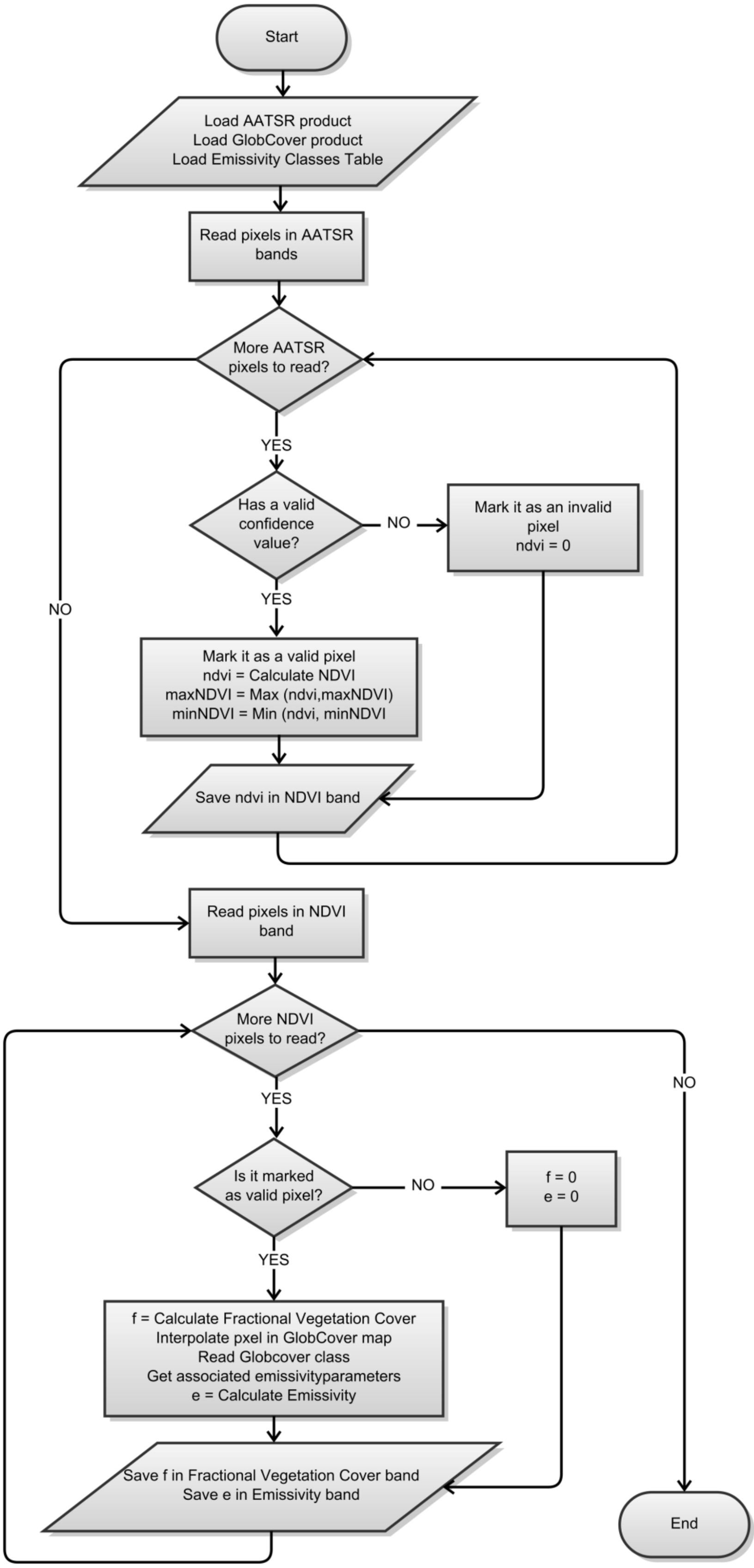

Figure 2.- Main flowchart of the system designed to produce emissivity maps for AATSR TIR channels.

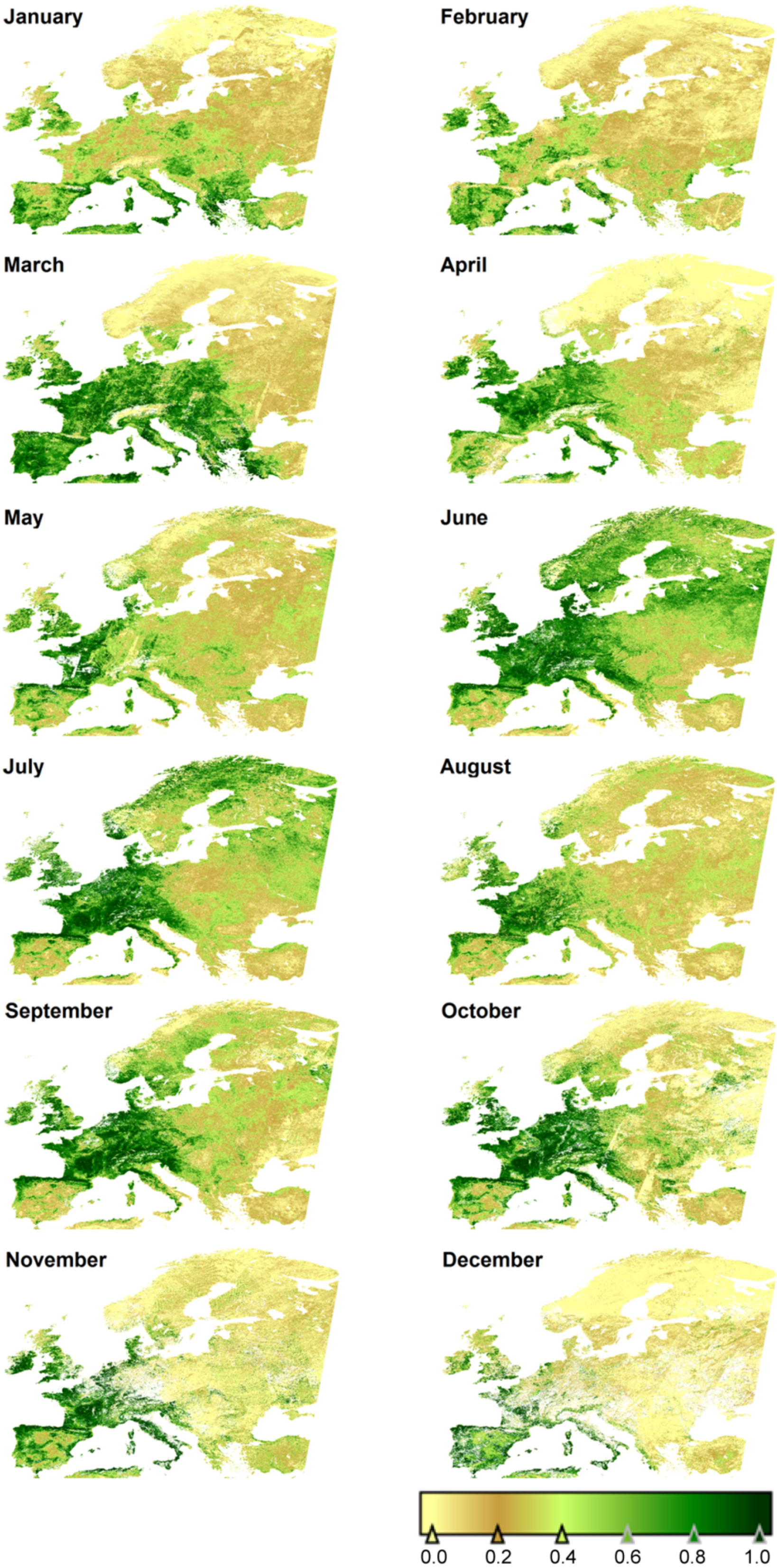

Figure 3.- Monthly fractional vegetation cover of Europe for year 2007. The monthly values have been calculated as the average of fractional vegetation covers over valid pixels in the considered month. White pixels correspond to water or cloudy areas.

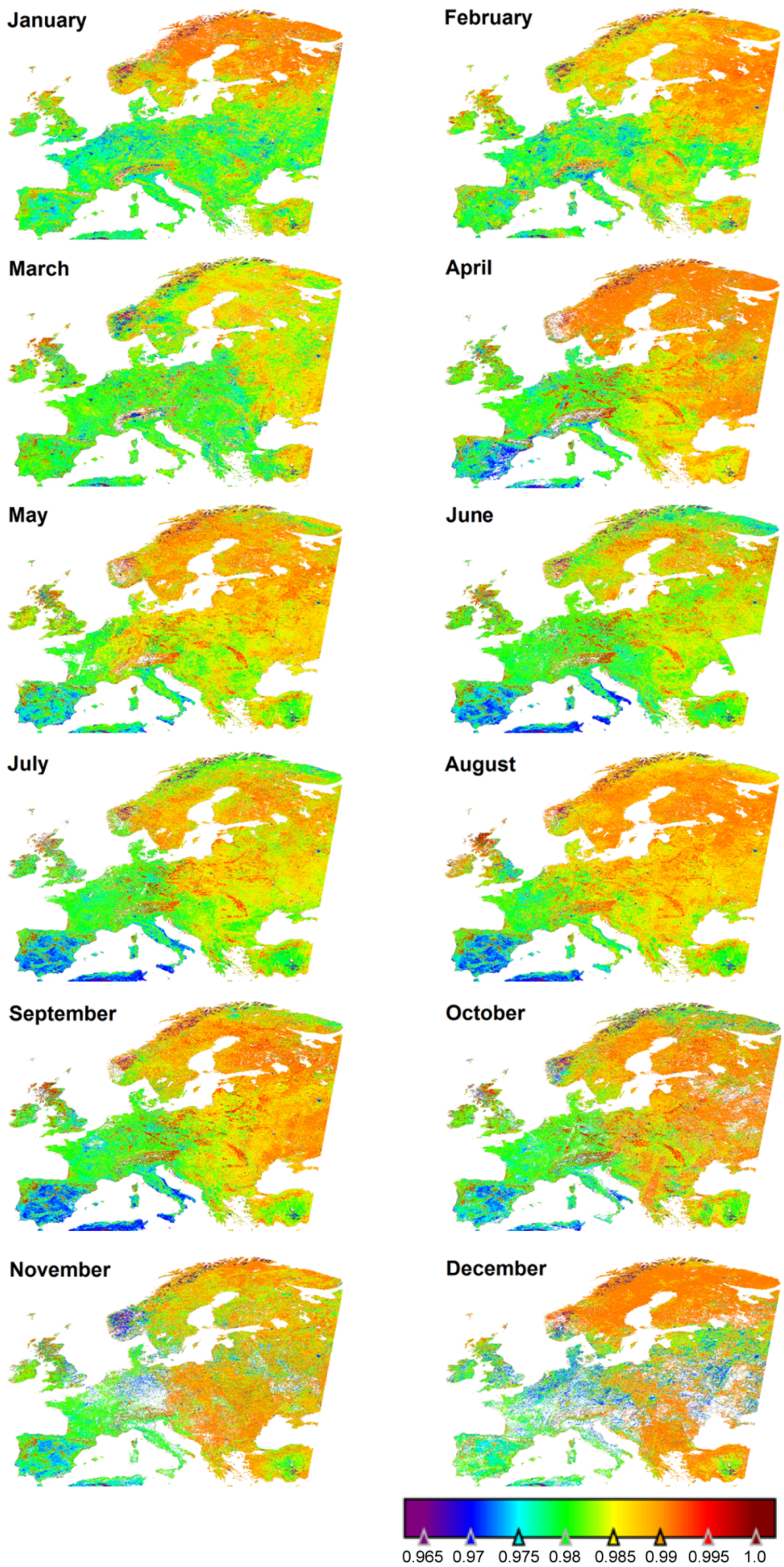

Figure 4.- Monthly emissivity in AATSR channel at 11 μm over Europe for year 2007. The monthly values have been calculated as the average of emissivities over valid pixels in the considered month.

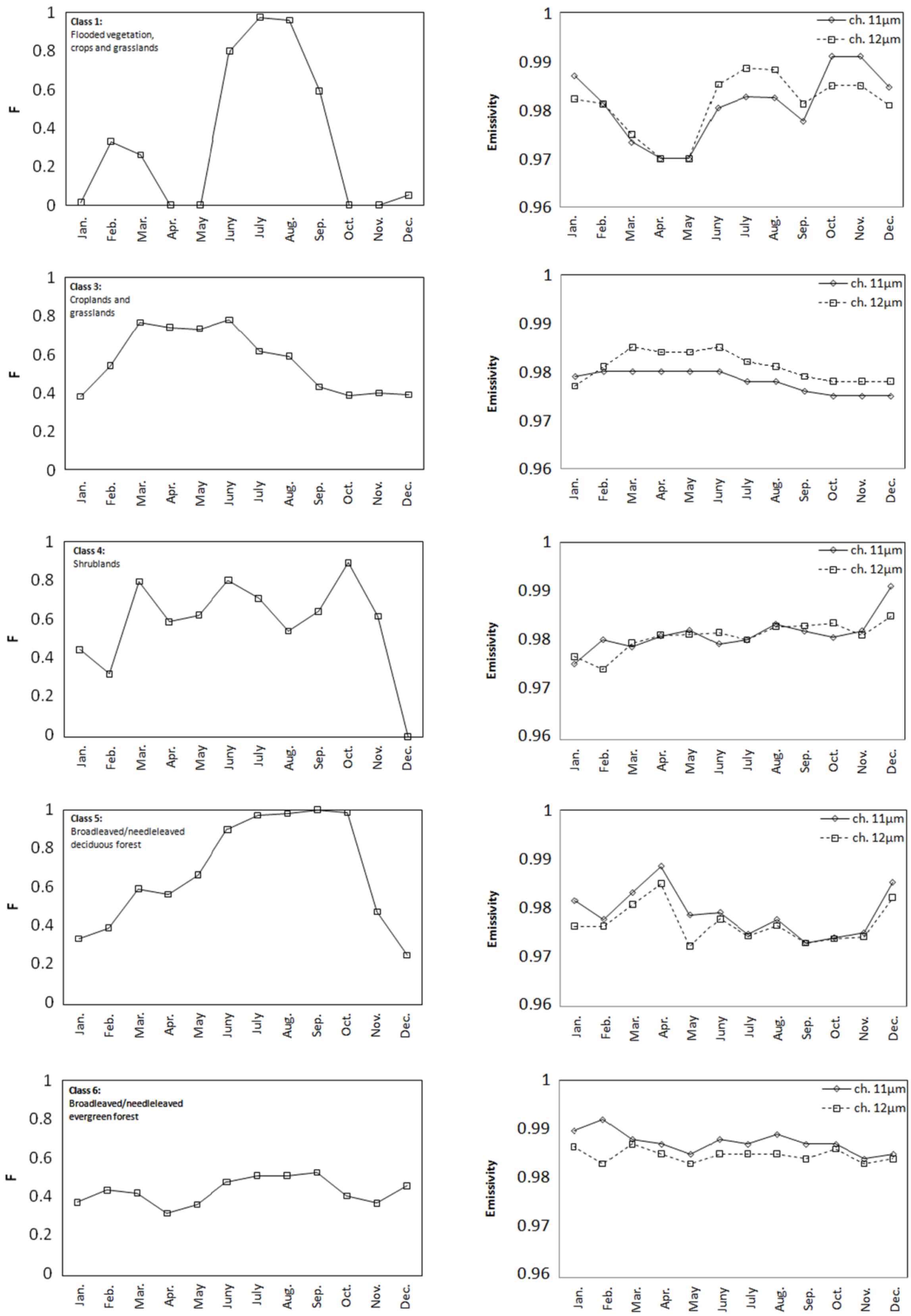

Figure 5.- Monthly evolution of fractional vegetation cover (graphs on the left) and emissivity (graphs on the right) for selected places corresponding to the different emissivity classes defined in Table 1 that are dependent on vegetation cover.

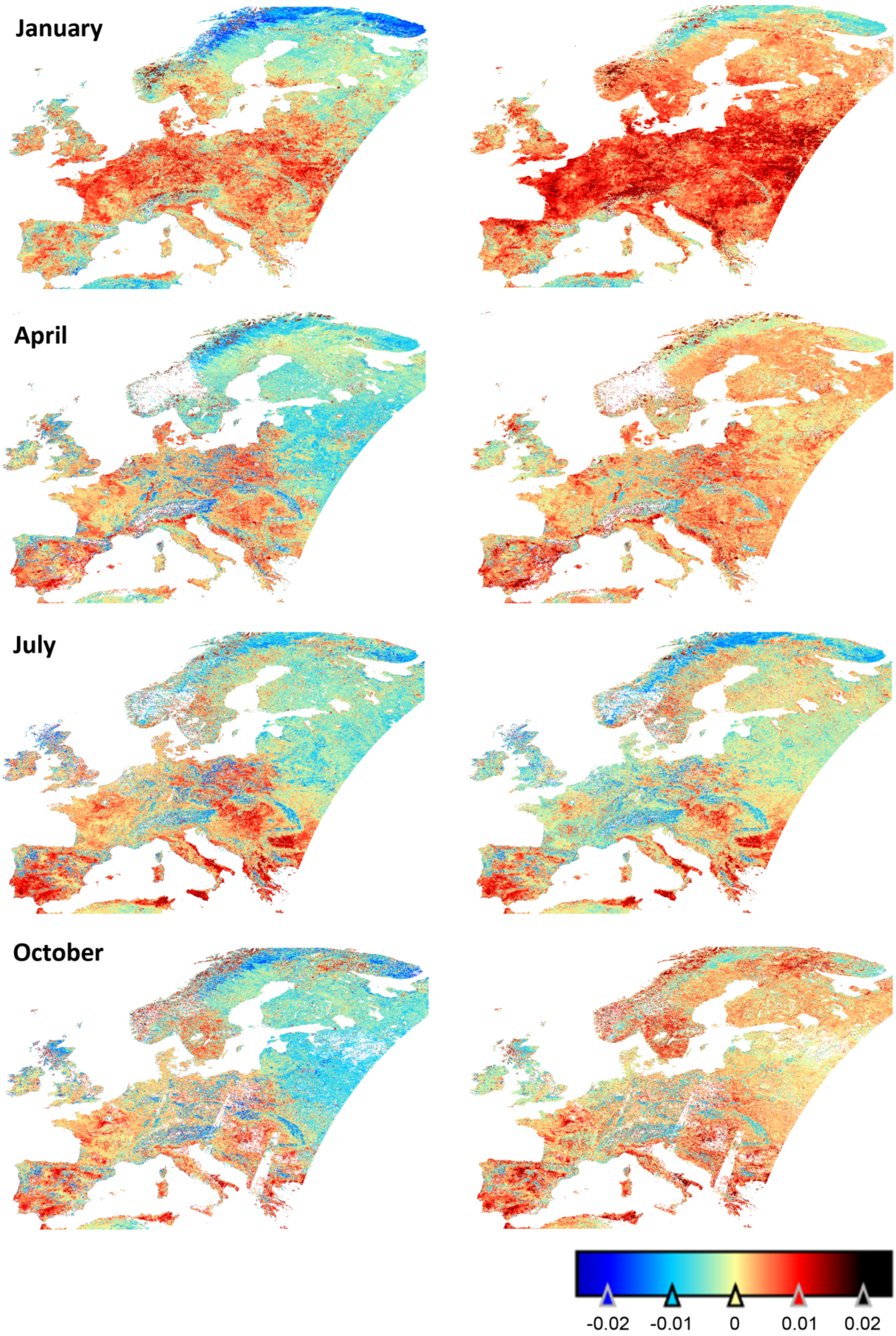

Figure 6.- Emissivity difference between the monthly emissivity estimates provided by the MODIS product MOD11-L2 and the AATSR product proposed in this paper (MODIS LSE – AATSR LSE) for the two split-window channels, corresponding to the months of January, April, July and October.

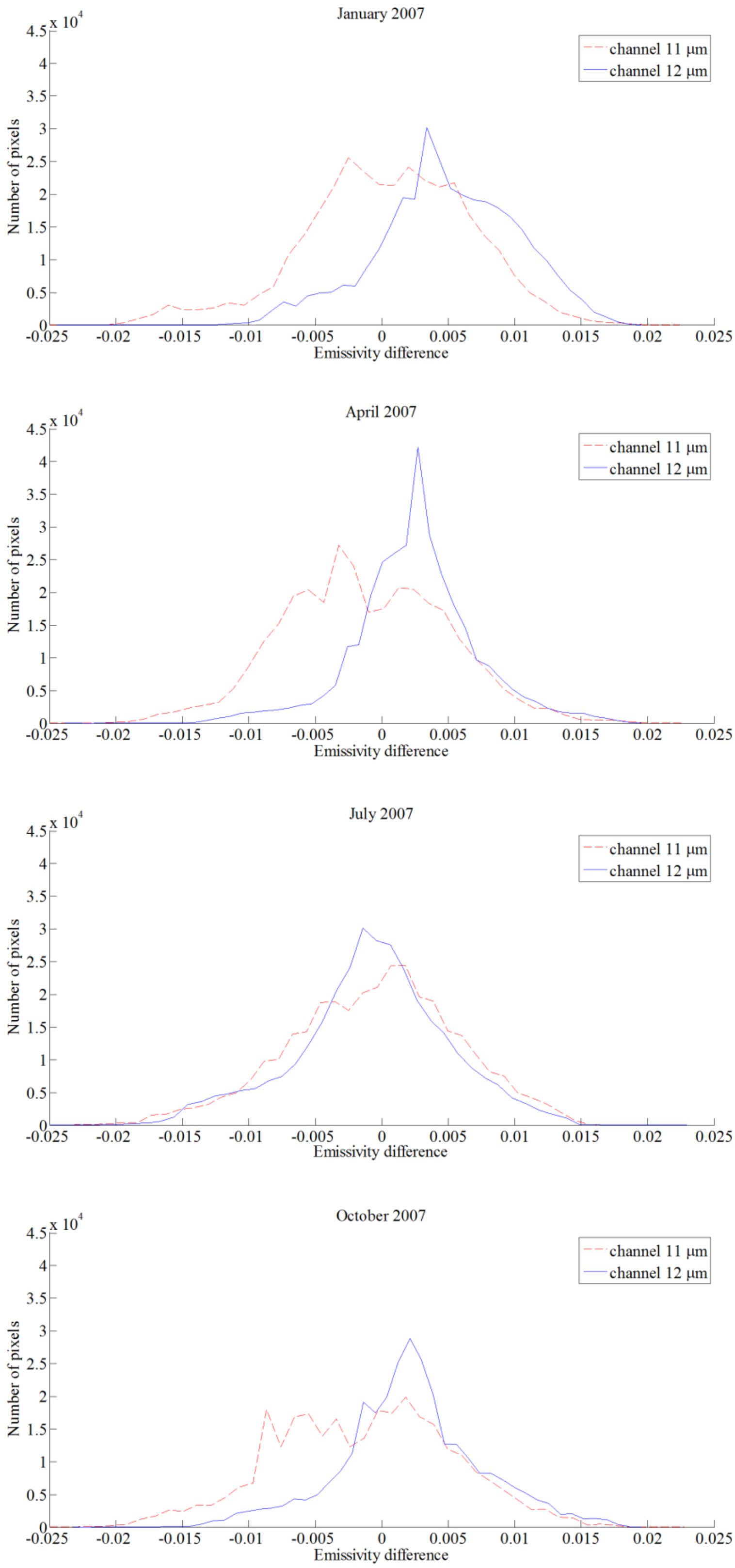

Figure 7.- Histograms of the emissivity differences between the monthly emissivity estimates provided by the MODIS product MOD11-L2 and the AATSR product proposed in this paper (MODIS LSE – AATSR LSE) for the two split-window channels, corresponding to the months of January, April, July and October.